

Acoustic thermometry of the western Mediterranean basin

E. K. Skarsoulis^{a)}

*Institute of Applied and Computational Mathematics, Foundation for Research and Technology Hellas,
P.O. Box 1527, 711 10 Heraklion, Crete, Greece*

U. Send

*Leibniz-Institut für Meereswissenschaften an der Universität Kiel, Düsternbrooker Weg 20, 24105, Kiel,
Germany*

G. Piperakis

*Institute of Applied and Computational Mathematics, Foundation for Research and Technology Hellas,
P.O. Box 1527 711 10 Heraklion, Crete, Greece*

P. Testor

*Leibniz-Institut für Meereswissenschaften an der Universität Kiel, Düsternbrooker Weg 20, 24105, Kiel,
Germany*

(Received 3 December 2003; revised 14 May 2004; accepted 15 May 2004)

Ocean acoustic tomography is used to obtain heat-content estimates for the western Mediterranean basin. Travel-time data from 13 tomography sections of the Thetis-2 experiment (January–October 1994) are analyzed with a matched-peak inversion approach. The underlying analysis involves the use of peak arrivals and nonlinear model relations between travel-time and sound-speed variations. Slice inversion results are combined with temperature covariance functions for the western Mediterranean to obtain heat-content estimates for the basin. These estimates compare favorably with ECMWF data over the nine-month period of the Thetis-2 experiment. Furthermore, estimates for the basin-average temperature of the western Mediterranean deep water are obtained. © 2004 Acoustical Society of America. [DOI: 10.1121/1.1771616]

PACS numbers: 43.30.Pc [AT]

Pages: 790–798

I. INTRODUCTION

The ability to monitor the heat content of ocean basins is important for understanding the role of the oceans in climate change, as well as for studying ocean variability and large-scale ocean processes. Although the upper ocean is routinely monitored on large scales by the existing operational ocean observing systems, such as satellite remote sensing and ARGO floats, there is a significant observational gap concerning the deep ocean. Moreover, there are shortcomings related with the resolution and coverage of the existing observing systems, such as the lack of vertical resolution of altimetry data and the low horizontal coverage by the ARGO system.^{1,2} These shortcomings/gaps can be resolved/filled by using acoustic monitoring techniques.

Ocean acoustic tomography was introduced by Munk and Wunsch^{3,4} as a remote-sensing technique for large-scale monitoring of the ocean interior using low-frequency sound. Measuring the travel/arrival times of pulsed acoustic signals propagating from a source to a distant receiver through the water mass over a multitude of different paths, and exploiting the knowledge about how travel times are affected by the sound-speed distribution in the water, the latter can be obtained by inversion. Further, sound speed is related to temperature,^{4,5} and, thus, ocean acoustic tomography can be used for the study of gyre- and basin-scale temperature and heat-content variability (acoustic thermometry).^{6,7}

An ocean acoustic tomography experiment called

Thetis-2 was conducted in the western Mediterranean from January to October 1994.⁸ The 9-month long experiment involved seven acoustic transceivers at a nominal depth of 150 m operating at 250/400 Hz, with a geometric configuration shown in Fig. 1. Acoustic travel-time data were collected along 13 tomographic sections with ranges between 220 and 610 km. The seasonal variability in the area gives rise to nonlinear relations between arrival-time and sound-speed variations.⁸ Furthermore, the lack of navigation data for one transceiver (W4) hampered the analysis of 4 tomographic sections originating at the particular transceiver. Preliminary heat-content results based on ray analysis of a single early arrival from 3 tomography sections were presented in a previous work.⁹ Due to the above mentioned factors the complete analysis of the full dataset (all arrivals, all sections) became feasible only after the development of improved modeling and analysis methods.

The application of an adaptive scheme¹⁰ based on the use of variable discrete background states, to be estimated from the tomography data rather than set *a priori*, enabled the efficient handling of nonlinear model relations. Further, the use of the peak-arrival approach^{11,12} for modeling travel-time observables enabled the exploitation of the latter independently of their identification as ray or modal arrivals. The introduction of a matched-peak inversion approach¹³ enabled the automatic analysis of travel-time data, bypassing the peak tracking and identification problem inherent in conventional analysis. Finally, an extended matched-peak approach made possible the analysis of the sections originating at W4,

^{a)}Electronic mail: eskars@iacm.forth.gr

by addressing the inversion problem along those sections simultaneously with the navigation problem for W4.¹⁴

In this paper we present results from the integrated analysis of the Thetis-2 dataset, and we combine tomographic sections to provide average temperature and heat-content estimates for the western Mediterranean sea. The heat-content estimates based on the analysis of the full acoustic dataset (13 sections, multiple arrivals) are a significant improvement to previous estimates based on inversions of a single early arrival along three sections⁹ in terms of both estimation accuracy (smaller errors) and agreement with estimates from independent heat-flux data. Furthermore, the exploitation of multiple arrivals adds vertical resolution to the inversion results.^{3,4} This allows estimates for the evolution of the deep-water temperature.

The contents of this work are organized as follows. In Sec. II we give a brief description of the matched-peak approach for slice inversions, along with the adaptive scheme for the treatment of nonlinear model relations. In Sec. III a minimum-variance linear estimator for the basin average temperature is derived in terms of temperature averages along sections. In Section IV presents the analysis results from the application of these methods to the acoustic dataset from the Thetis-2 tomography experiment. The main conclusions from this work are presented and discussed in Sec. V.

II. MATCHED-PEAK SLICE INVERSION

The solution of the forward problem in ocean acoustic travel-time tomography leads to a set of model relations,

$$\tau_i = g_i(\vec{\vartheta}), \quad i = 1, \dots, I, \quad \vec{\vartheta} \in \Theta, \quad (1)$$

nonlinear in general, between the arrival times τ_i , $i = 1, \dots, I$ (I is the number of arrivals) and the sound-speed parameter vector $\vec{\vartheta} = (\vartheta_1, \dots, \vartheta_L)$, made, e.g., of the amplitudes of the modes parametrizing the sound-speed profile; Θ denotes the parameter domain. Arrival times can be defined modeled in various ways using, e.g., the notions of ray, modal, or peak arrivals.^{4,11} Linearizing the relations (1) about a set of background states $\vec{\vartheta}^{(b)}$, $b \in B$, with corresponding arrival times $\tau_i^{(b)} = g_i(\vec{\vartheta}^{(b)})$, and, further, discretizing the local parameter space, about each background state, into a local grid with index $k \in K$, the following relations can be obtained:

$$\begin{aligned} \tilde{\tau}_i(b, k) &= \tau_i^{(b)} + \sum_{l=1}^L \frac{\partial g_i(\vec{\vartheta}^{(b)})}{\partial \vartheta_l} [\tilde{\vartheta}_l(b, k) - \vartheta_l^{(b)}], \\ i &= 1, \dots, I, \quad b \in B, \quad k \in K, \end{aligned} \quad (2)$$

where $\{\tilde{\vartheta}_l(b, k)\}$ represent the discrete model states, and $\{\tilde{\tau}_i(b, k)\}$ the corresponding arrival times. Using the relations (2), the arrival times corresponding to a set of discrete model states spanning the parameter space Θ can be calculated rapidly, since the full arrival-pattern calculations need to be carried out at a limited number of background model states $\vec{\vartheta}^{(b)}$, $b \in B$. The derivatives $\partial g_i(\vec{\vartheta}^{(b)})/\partial \vartheta_l$, called influence coefficients, can be expressed and calculated in terms of background quantities and sound-speed modes.^{4,11} Depending on the background state b and the discretization steps $\delta\vec{\vartheta}$, an estimate for the upper bound of the prediction

error ϵ_i can be obtained¹³ as a sum of a discretization error and an observation/modeling error n_i ,

$$\begin{aligned} \epsilon_i(b, \delta\vec{\vartheta}) &= \frac{1}{2} \sum_{l=1}^L \left| \frac{\partial g_i(\vec{\vartheta}^{(b)})}{\partial \vartheta_l} \delta\vartheta_l \right| + n_i, \\ i &= 1, \dots, I, \quad b \in B, \end{aligned} \quad (3)$$

The observed arrival times $\tau_j^{(o)}$, $j = 1, \dots, J$ are allowed to associate with the model arrival times $\tilde{\tau}_i(b, k)$ if their time difference is smaller than the tolerance $\epsilon_i(b, \delta\vec{\vartheta})$. Finally, those model states are selected that maximize the number of associations between observed and model peaks.

Besides the ocean variability, represented by the model state $\{\tilde{\vartheta}_l(b, k)\}$, there are also other sources of variability, such as mooring motion. In this case the model relations can be written in the following linearized form:

$$\begin{aligned} \tilde{\tau}_i(b, k; \delta r) &= \tau_i^{(b)} + \sum_{l=1}^L \frac{\partial g_i(\vec{\vartheta}^{(b)})}{\partial \vartheta_l} [\tilde{\vartheta}_l(b, k) - \vartheta_l^{(b)}] \\ &\quad + \frac{\partial \tau_i}{\partial r} \delta r, \end{aligned} \quad (4)$$

where r is the source–receiver range and δr represents the range variation due to mooring motion, which is a function of time. The mooring motion is usually estimated from additional navigation data, and its effect is removed from the observed travel times prior to the analysis. However, in the case of missing navigation data, as in the case of W4, the correction cannot be calculated/applied *a priori*.

The matched-peak approach can be extended to estimate δr together with the ocean state, by maximizing the number of peak associations as a function of the model state (b, k) and the range variation δr . In the case of the four Thetis-2 sections involving W4 the simultaneous transmissions along the four sections can be exploited to obtain better estimates; in that case the quantity to maximize is the joint number of peak associations along all sections.¹⁴

III. HORIZONTAL AVERAGE

For heat-budget studies it is desirable to obtain estimates for the average temperature (heat content) over a sea area, in order to balance its evolution with the surface heat fluxes and fluxes through the side boundaries.¹⁵ Tomography provides estimates for the range-average temperature along a number of transmission lines defined by the geometry of the tomographic array for different layers in depth. Considering a temperature field $T(x, y)$ over an area A of size $|A|$, an optimal estimator is sought for the horizontally average temperature H ,

$$H = \frac{1}{|A|} \int_A T(x, y) dx dy, \quad (5)$$

in terms of the temperature averages D_m along a number of lines S_m (of length L_m), $m = 1, \dots, M$, representing tomography sections,

$$D_m = \frac{1}{L_m} \int_{S_m} T(x(s), y(s)) ds. \quad (6)$$

The vertical dependence is omitted here for simplicity, but one can consider T as the vertically averaged temperature over a certain layer. The range-average temperature along a tomography section at a particular depth is directly related with the corresponding average sound speed, which, in turn, is related through the parameter vector ϑ and the model relations (2) with the tomographic travel-time observables.

Taking the simplest case of a linear estimator of the horizontal average,

$$\hat{H} = \sum_{m=1}^M a_m D_m, \quad (7)$$

where a_m are unknown weights, and assuming it to be a minimum-variance estimator the following system of equations can be obtained by setting the derivatives of the variance $\langle (\hat{H} - H)^2 \rangle$, with respect to a_m , equal to zero:

$$\sum_{k=1}^M a_k \langle D_m D_k \rangle = \langle H D_m \rangle, \quad m = 1, \dots, M. \quad (8)$$

This system can be solved for the weights $\mathbf{a} = \{a_m\}$, which can be thus expressed in terms of $\mathbf{C}_{DD} = \{\langle D_m D_k \rangle\}$, the covariance matrix between the line averages (data), and $\mathbf{c}_{HD} = \{\langle H D_m \rangle\}$, the covariance vector between the horizontal and the line averages,

$$\mathbf{a} = \mathbf{C}_{DD}^{-1} \mathbf{c}_{HD}. \quad (9)$$

The mean square error (error variance) then becomes

$$\langle (\hat{H} - H)^2 \rangle = \langle H^2 \rangle - \mathbf{c}_{HD}' \mathbf{C}_{DD}^{-1} \mathbf{c}_{HD}, \quad (10)$$

where a prime denotes transposition. The covariance matrix \mathbf{C}_{DD} and covariance vector \mathbf{c}_{HD} can be calculated from the temperature covariance function $\langle T(x', y') T(x, y) \rangle$,

$$\begin{aligned} \langle D_m D_k \rangle &= \frac{1}{L_m L_k} \int_{S_m} \int_{S_k} \langle T(x(s_m), y(s_m)) T(x(s_k), y(s_k)) \rangle \\ &\quad \times ds_m ds_k, \end{aligned} \quad (11)$$

$$\begin{aligned} \langle H D_m \rangle &= \frac{1}{|A| L_m} \int_A \int_{S_m} \langle T(x', y') T(x(s_m), y(s_m)) \rangle \\ &\quad \times dx' dy' ds_m. \end{aligned} \quad (12)$$

The variance $\langle H^2 \rangle$ can be calculated similarly. By assuming the temperature field to be homogeneous, i.e., by considering the temperature covariance to be a function of the distance between the points (x', y') and (x, y) , the above expressions can be further simplified.

IV. ANALYSIS OF THETIS-2 DATA

Analysis of historical temperature data for the area covered by the Thetis-2 experiment (1° – 9° E) resulted in a set of empirical orthogonal functions (EOFs). The first three EOFs, shown in Fig. 1, with rms amplitudes 18.48, 2.88, and 0.96, respectively, explain 99.6% of the anticipated variance concentrated mostly in the upper layers. Two systematic CTD surveys conducted in January and October 1994 (R/V Poseidon and R/V Suroit cruises) revealed significant deviations

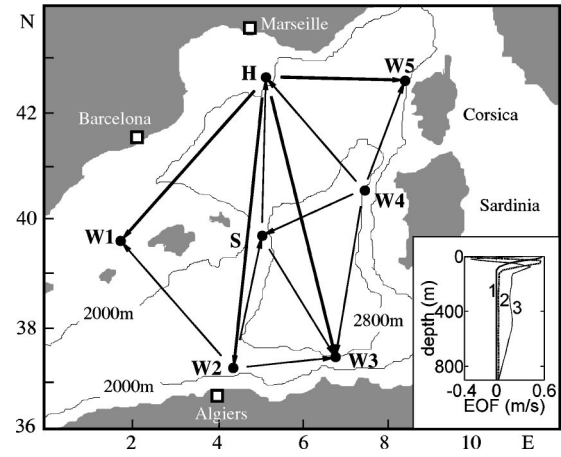


FIG. 1. The geometry of the Thetis-2 tomography experiment in the western Mediterranean sea and the first 3 EOFs for the area of interest (bottom right).

from the climatological mean conditions at large depths: the average 1994 temperatures below 600 m were about 0.05°C higher than the 40-year historical mean. Because of that the reference sound-speed profile for the inversions in the deep layers was calculated from the CTD data rather than from the climatology. While the variability in the upper layers can be sufficiently described by the first three EOFs shown in Fig. 1, the description of the deep layers would require a larger number (>15) of higher-order EOFs. In order to keep the number of parameters low, the deep-water variability is described here by two additional box-shaped modes covering the 600–1000 and 1000–2000 m layer, respectively—the depth of 1000 m separates two main water masses: the Levantine intermediate water (LIW) and the western Mediterranean deep water (WMDW).¹⁶ The three EOFs shown above are truncated below 600 m, such that the parametric description of the upper and the deeper layers is uncoupled. The variability of the CTD data along the tomography sections in the 600–1000 and 1000–2000 m layer is 0.14 and 0.02 m/s rms, respectively, on average.

It is known from previous works^{8,13,14} that the seasonal variability associated with EOF-1 variations, confined in the upper 100 m, gives rise to a significant nonlinearity of the model relations, due to the passage from surface-reflected propagation conditions in winter to refracted propagation in the summer. The extent of the nonlinearity is such that the use of a single background state (annual mean) would give rise to linearization errors as large as 300 ms for intermediate arrivals of longer sections over the EOF-1 variability interval. By using a set of discrete background states with respect to ϑ_1 this error can be drastically reduced: taking the discretization step $\delta\vartheta_1 = 2$, the error becomes less than 2 ms, better than the travel-time measurement accuracy (8 ms). The background state appropriate for each tomographic reception is estimated from the inversion, as described in Sec. II, rather than set *a priori*, e.g., from the monthly climatology.¹⁷ Still, the monthly climatology is useful for defining appropriate search intervals for the background state estimation, thus reducing the computational burden significantly.¹³ The parameter domain Θ is taken as the Cartesian product of the parameter intervals for the amplitudes

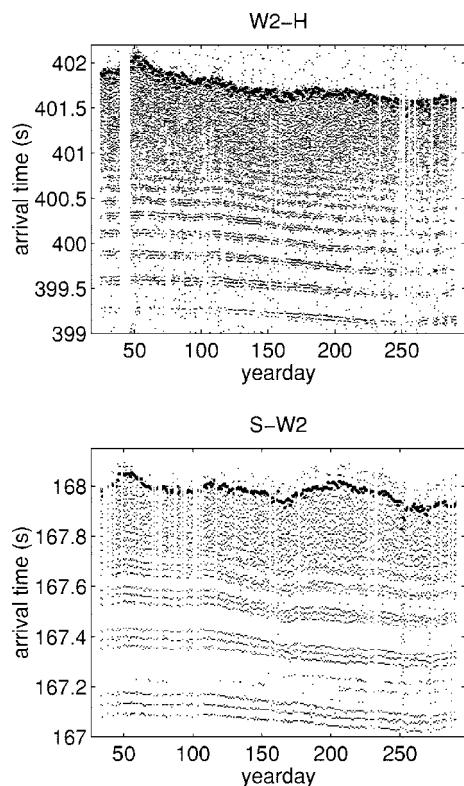


FIG. 2. Measured travel-time data along the sections W2-H and S-W2 over the nine-month duration of the experiment. The heavier dots denote cut-off peaks.

of the sound-speed modes, each one covering ± 2.5 standard deviations (rms values) of the EOF amplitudes and sound-speed anomalies.

A. Slice inversions

Figure 2 shows the travel-time data from two characteristic sections of the Thetis-2 experiment, a long section from H to W2 (605 km) and a short one from W2 to S (253 km), after correlation (matched-filter) processing, clock-drift correction, mooring-motion correction, offset calibration and incoherent one-day averaging of arrival patterns.⁸ The horizontal axes represent yeardays of 1994 and span the nine-month period of the experiment, whereas the vertical axes measure the arrival time in seconds. Early arrivals corresponding to steep propagation angles arrive in groups of three (arrival triplets). Later groups of arrivals get closer and overlap with each other such that their identification, e.g., in terms of ray arrivals, becomes a problem. The most characteristic feature of the late arrival pattern is the abrupt end of the reception following the typical crescendo in the intensity of late arrivals.⁴ The cut-off peaks, defined as the last of the five highest peaks in each reception, are shown in Fig. 2 through the heavier dots. Additional peaks in Fig. 2 are due to noise or due to bottom-interacting acoustic energy. Further, it is seen from Fig. 2 that there are periods of poor data quality or absence of data; these are periods of low signal/noise ratio (SNR).

The geometry of eigenrays sampling the sections W2-H and S-W2, calculated for the annual mean sound-speed profile, is shown in Fig. 3, to highlight the effectiveness of the

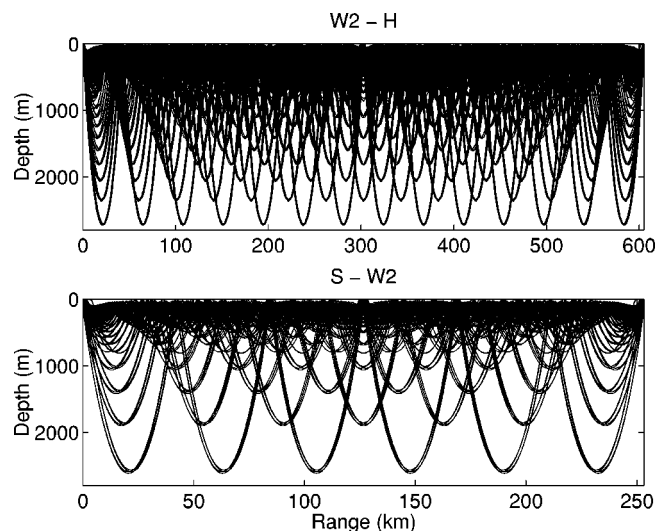


FIG. 3. Geometry of eigenrays along the sections W2-H and S-W2 (calculation based on the annual mean sound-speed profile).

horizontal averaging implicit in the tomography sampling. Above 2000 m, which is the maximum depth analyzed in this paper, the largest horizontal gaps (unsampled regions) are of the order of 30 km, but more typically approximately 10 km. Most of the ocean variability is in mesoscale and large-scale fields, with scales of 100 km and higher, as presented in the next subsection, so good horizontal averages are expected from the tomography travel-time data. The steep rays penetrating the deep layers in Fig. 3 correspond to the early arrivals in Fig. 2 and the shallow rays to the late arrivals. The eigenrays are grouped in bundles of four characterized by similar arrival times (two of which are identical⁴) and corresponding to the arrival triplets in Fig. 2.

For every tomography section influence coefficients were calculated for all arrivals (relative maxima) at the various background states using the peak-arrival approach.¹³ The arrivals that could be continuously traced over the entire range of anticipated variability (over the different background states) were used as the model arrivals to be associated with the observed ones in the matched-peak inversion. Those contain the distinguishable groups of early arrivals followed by a number of intermediate arrivals and finally the cut-off peak. The observation errors for the early and intermediate arrivals were set equal to 10 ms, close to the travel-time measurement accuracy. Late arrivals and, in particular, the cut-off peak are subject to range-dependence effects.¹⁸ The reason is that these arrivals sample the shallow water layers where range dependence is strongest. From the study of large-scale range-dependence effects on travel times along the Thetis-2 sections bias and variability estimates were obtained for the cut-off arrival times; the effects on the early and intermediate arrivals were small compared to the observation accuracy, whereas for the cut-off travel-times biases between 50 and 200 ms (delay bias) and residual variability between 50 and 100 ms rms were observed.¹⁸ These effects on the cut-off arrival times are taken into account in the following range-independent inversions by correcting for the bias and increasing the observation error for the cut-off peak to 50–100 ms, depending on the section.

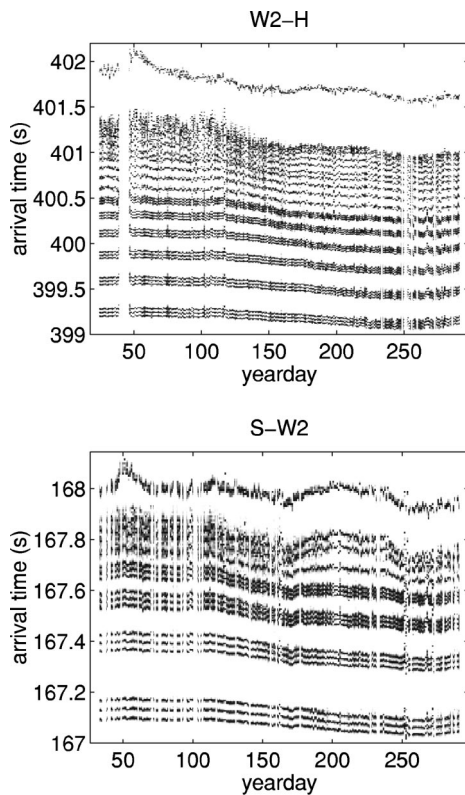


FIG. 4. The *a posteriori* probability density functions (pdfs) of peak arrival times (theoretical arrival times) for the sections W2-H and S-W2, corresponding to the population of selected model states for each reception. A gray scale is used for the representation of each pdf, with white representing zero density and black representing the density maximum.

Figure 4 shows the *a posteriori* probability density functions (pdfs) of peak arrival times for the sections W2-H and S-W2 after the application of the matched-peak inversion approach. The analysis of each reception leads to a population of model states (background states and perturbations). For each model state the corresponding arrival times can be calculated from the model relations, and, thus, a population of travel times can be obtained for each arrival. Figure 4 shows the pdfs for the travel-time populations for the theoretical arrivals used in the W2-H and S-W2 inversions. It is seen that the travel-time data (Fig. 2) are well reproduced by the model results (Fig. 4), even though in a weak (distribution) sense. The quality of the inversion depends on the qual-

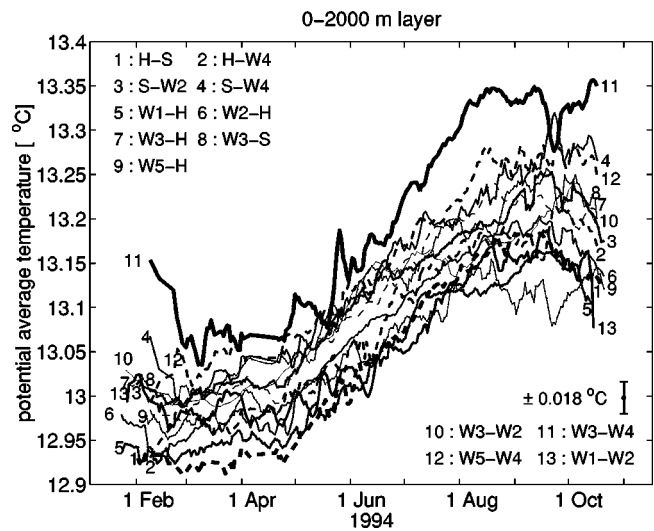


FIG. 5. Inversion results from individual sections for the 0–2000 m layer. The different sections are identified by numbers (1–13) and different line types. The average rms inversion error for all sections (0.018 °C) is plotted (bottom right), whereas the individual inversion error for each section is given in Table I (rightmost column).

ity of the data; low SNR data lead to poor inversion quality. The identification of the individual intermediate arrivals following the distinct arrival triplets are associated with larger ambiguity, depending on the separability of adjacent peaks in the measured travel-time data. In this connection, the inclusion of additional peaks with small separability in the inversions will have no substantial contribution to the information content. An important feature of the matched-peak approach is that it applies to any reception, independently of previous inversion results or initial conditions. This enables the analysis of data even in the presence of large gaps. On the other hand, a problematic reception/inversion will not at all affect the analysis of subsequent receptions.

Figure 5 shows the slice inversion results for the individual sections in the form of potential temperatures averaged over the 0–2000 layer. The inversion errors for the various sections/layers are summarized in Table I; in Fig. 5 only the average rms error for all 13 sections (0.018 °C rms) is plotted. A typical seasonal trend is observed in the inversion results of Fig. 5 along all sections. The seasonal cycle though confined in the upper water layer has a significant

TABLE I. Average rms inversion errors (°C) for the 13 Thetis-2 sections in various depth layers.

Layer (m):	0–50	50–100	100–200	200–400	400–600	600–1000	1000–2000	0–2000
H-S	0.5810	0.2874	0.0515	0.0475	0.0574	0.0468	0.0124	0.0168
H-W4	0.5278	0.3158	0.0808	0.0626	0.0649	0.0487	0.0116	0.0219
S-W2	0.5689	0.3209	0.0683	0.0496	0.0505	0.0462	0.0122	0.0169
S-W4	0.5834	0.3461	0.0867	0.0620	0.0597	0.0502	0.0125	0.0244
W1-H	0.5810	0.2356	0.0533	0.0456	0.0512	0.0414	0.0127	0.0162
W1-W2	0.6634	0.3609	0.0710	0.0494	0.0509	–	–	0.0337
W2-H	0.5854	0.3327	0.0493	0.0420	0.0508	0.0471	0.0117	0.0130
W3-H	0.5053	0.2870	0.0646	0.0504	0.0541	0.0436	0.0102	0.0100
W3-S	0.5784	0.3699	0.0833	0.0563	0.0505	0.0541	0.0116	0.0156
W3-W2	0.5850	0.3318	0.0779	0.0566	0.0562	0.0522	0.0126	0.0157
W3-W4	0.4950	0.2983	0.0716	0.0533	0.0541	0.0458	0.0079	0.0190
W5-H	0.5708	0.2816	0.0681	0.0547	0.0581	0.0488	0.0116	0.0155
W5-W4	0.5264	0.3485	0.0646	0.0484	0.0525	0.0454	0.0098	0.0187

signature in the average over the whole water column. Apart from the seasonal signal the spatial spread, i.e., the variability between the various sections, is also significant and nearly as large as the seasonal signal. The inversion results from two sections, W3–W4 and H–S, are highlighted in Fig. 5, through heavy solid and dashed lines, respectively. The section W3–W4 in the southeast is by far the warmest, as far as the whole water column is concerned. This is due to the inflow of warm water masses from the eastern Mediterranean, in particular, of the Levantine intermediate water. On the other hand, the section H–S is among the coldest. This section partly covers the Gulf of Lions, where deep convection takes place in winter.¹⁹

Table I presents the average inversion errors for the various layers along the Thetis-2 sections. The errors are larger for the shallow layers and smaller for the deep layers, in agreement with the larger variability anticipated at shallow depths. The temperature anomalies in the various depth layers are not statistically independent. Therefore, the variance of the average temperature in the 0–2000 m layer is not simply a sum of variances of the contributing layers scaled by the layer thicknesses; cross-terms are important and have to be accounted for. In general, the inversion errors decrease with an increasing source–receiver range but they also depend on data quality. The largest errors are observed along the section W1–W2. This section samples depths up to 600 m due to energy stripping taking place at the Balearic sill between Mallorca and Ibiza. As a result, the receptions lack the clear identifiable groups of early arrivals and this has an impact on the inversion errors. The error estimate for the 0–2000 m layer in this case was obtained, assuming zero variability for depths larger than 600 m. Further, large errors, especially for the deep layers, are observed along the sections H–W4 and S–W4 for which the inversion problem is solved together with the navigation problem of W4. The other two sections involving W4 (W3–W4 and W5–W4) have significantly smaller errors; the reason is that these two sections have about the same orientation such that the W4-mooring-motion effects on arrival times are strongly correlated in the two datasets.

B. Horizontal averages

By combining inversion results from the 13 sections, three-dimensional temperature averages for the area covered by the Thetis-2 tomographic array (1° – 9° E) are presented in this section. To obtain the optimal (minimum-variance) linear estimator, covariance functions from temperature data were calculated. The temperature anomalies were assumed to be spatially homogeneous, i.e., the covariance of temperature anomalies was treated as a one-dimensional function of the horizontal distance between any two locations.

For the 0–2000 m layer, a superposition of two Gaussian models was used to represent the one-dimensional temperature covariance function covering large- and mesoscale structures. The covariance function of the large-scale seasonal temperature fluctuations was obtained from historical seasonal data for the area of interest after subtraction of the local time-mean values. This one-dimensional covariance function reveals dominant large-scale structures of 300 km

TABLE II. Weights for the minimum-variance estimator of the horizontal average temperature in the 0–2000 and 600–2000 m layers.

Layer (m):	0–2000	600–2000
H-S	–0.0128	0.0349
H-W4	0.0182	0.0265
S-W2	–0.0110	0.0567
S-W4	0.0514	0.0316
W1-H	0.1858	0.1083
W1–W2	0.1544	0
W2-H	0.1355	0.0077
W3-H	0.0384	0.0442
W3-S	0.0503	0.0239
W3–W2	0.0667	0.0429
W3–W4	0.1275	0.0665
W5-H	0.1031	0.0526
W5–W4	0.0906	0.0514

scale dominated by the seasonal variability. Then the departures from the seasonal means at different locations were calculated and grouped according to their horizontal distance to calculate a mesoscale covariance function. This covariance function of the mesoscale temperature fluctuations has a scale of 100 km. These values were also found to be consistent with data from a high-resolution numerical model of the western Mediterranean.²⁰ Table II (mid-column) presents the weights of the resulting minimum-variance linear estimator for the horizontal average temperature in the 0–2000 m layer. The estimation error of the three-dimensional average for this layer is 0.0025°C rms.

Figure 6 shows the evolution of the average temperature over the area 1° – 9° E in the layer 0–2000 m (heavy solid line) estimated from the inversion results along the 13 Thetis-2 sections shown in Fig. 5. The rms error (shaded

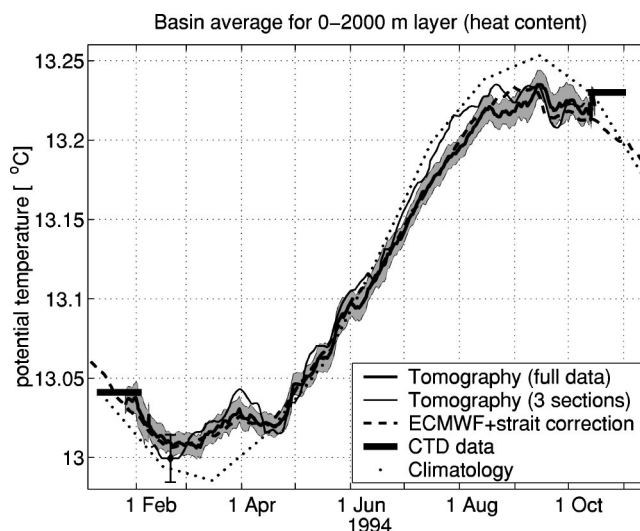


FIG. 6. Evolution of the average temperature of the upper 2000 m of water in the western Mediterranean (1° – 9° E) estimated from tomography (solid lines) and ECMWF heat-flux data (dashed line), and compared with the seasonal cycle from the climatology (dotted line). The CTD data from the Poseidon/Suroit cruises in January/October are also shown (horizontal bars). The heavy solid line and the shaded area represent the mean tomography estimate and rms error from the complete analysis of the 13 Thetis-2 sections. The light solid line and vertical error bar represent earlier tomography results based on the analysis of a single early arrival along three sections (W1–H, W3–H, and W5–H).

area), integrating the inversion error and the error of the averaging process, is variable depending on the quality of data; its average value is 0.0081°C . The heavy horizontal bars in January and October represent the average temperatures from the Poseidon and Suroit CTD data, respectively; the horizontal extent of the bars represents the time spread of these data. The dashed line in Fig. 6 shows the integral of independent heat-flux data, i.e., the total input of heat into the basin through the surface converted to volume-average temperature, for the western Mediterranean basin, obtained from the European Center for Medium-range Weather Forecasts (ECMWF). The ECMWF heat-flux data for the entire western basin were corrected by 5.7 W/m^2 to account for heat transport through the Sicily/Gibraltar straits—there is a net heat influx through the straits—and the resulting temperature amplitude was adjusted (scaled by 92.5%) to a smaller seasonal amplitude for the 1° – 9°E subregion.⁹ The agreement of the tomography results and the ECMWF data is surprisingly good, not only on annual time scale but also seasonally and reproducing many short term events, such as a warming interruption in April and a strong cooling in mid September. The deviations of the ECMWF data are in most cases within the error bars of the tomography results.

The dotted line in Fig. 6 represents the seasonal cycle in the 1° – 9°E area for the 0–2000 m layer resulting from the monthly mean climatology, up to a constant. The seasonal amplitude from the climatology is about 20% higher than the ECMWF flux integral and the tomography results. This indicates that the *a priori* setting of a time-variable background state for tomographic inversions based on the climatology could have led to significant biases. Earlier tomography estimates, based on inversions of a single early arrival along three sections (W1-H, W3-H, and W5-H)⁹ are also plotted in Fig. 6 for comparison. The corresponding rms error is 0.015°C , about twice as large as the error from the latest estimates; the error remains constant in this case. In connection with the larger errors, the deviation from the ECMWF heat-flux integral is also significantly larger than in the latest results.

Average temperature estimates for the 600–2000 m layer, i.e., for the western Mediterranean deep water, are presented in the following. Due to the sparseness of historical data for this layer the temperature covariance function was calculated using data from a large number of profiling floats deployed by IfM Kiel in the western Mediterranean from 1997 to 2002. Again a two-scale Gaussian model was fitted to the one-dimensional covariance function, revealing dominant structures of 100 and 12 km scales, respectively, i.e., the correlation lengths are significantly smaller than for the 0–2000 m layer. The reason is the absence of the seasonal signal at depth. The mesoscale is the same in both layers, but in addition here submesoscale features are captured (e.g., submesoscale coherent vortices, so-called SCV's, fronts, filaments, etc.). Probably the additional very short scales become more visible here since at depth they are not dominated by the large seasonal variability. Table II (rightmost column) presents the weights of the minimum-variance linear estimator for the horizontal average temperature in the 600–2000 m layer. The estimation error of the 3-D average for this layer is

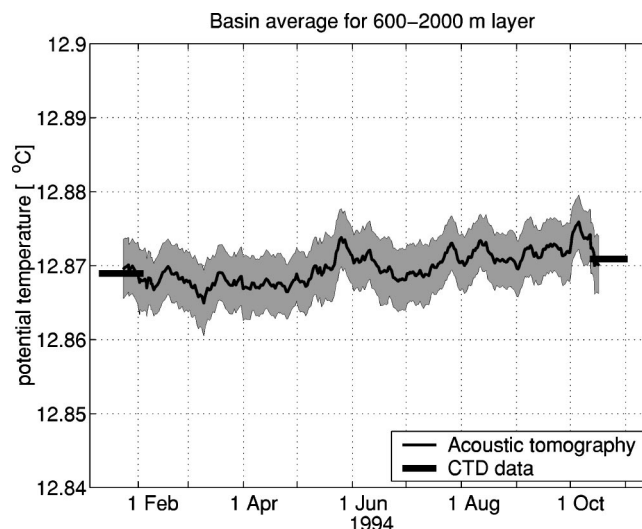


FIG. 7. Evolution of the average temperature in the deep water (600–2000 m layer) of the western Mediterranean basin (1° – 9°E) estimated from acoustic tomography; the solid line represents the mean and the shaded area the rms error. CTD data from the Poseidon/Suroit cruises in January/October are shown as horizontal bars.

0.0024°C rms. Figure 7 shows the average temperatures over the area 1° – 9°E for the deep layer (600–2000 m). The rms error, represented by the shaded area, has an average value of 0.0038°C ; this is the accuracy of the Thetis-2 configuration for the deep-water temperature measurement. The average temperatures from the Poseidon and Suroit CTD data in January and October are also shown in Fig. 7 and they agree with the tomography results.

A previous analysis of long-term historical *in situ* observations in some parts of the western Mediterranean basin revealed a long-term warming trend of the deep water by $\sim 0.003^{\circ}\text{C}/\text{year}$.²¹ However, it was not clear from these studies how widespread this signal was. Over a period of nine months, such a trend would give a temperature increase of 0.0022°C . The difference of the basin-average temperatures in the CTD data from January (Poseidon) to October (Suroit) in Fig. 7 is about 0.0019°C , which is very close to the above estimate. Some of this agreement may be spurious, but it is not inconsistent with the hypothesis of a basin-wide warming trend for the western Mediterranean deep water. Further, as mentioned before, the average 1994 temperatures below 600 m, estimated from the Poseidon/Suroit CTD data, were about 0.05°C higher than the 40-year historical mean; this is also compatible with a basin-wide warming trend of $0.003^{\circ}\text{C}/\text{year}$. An indication of a basin-wide warming trend can be seen in the tomography results as well. Nevertheless, the anticipated temperature difference (0.0022°C) over the nine months is smaller than the tomography error (0.0038°C), and, in this connection, longer-term (\geq two-year) tomography measurements would be necessary to draw more reliable conclusions.

V. DISCUSSION AND CONCLUSIONS

Results from an integrated analysis of the complete set of travel-time data from the Thetis-2 tomography experiment were presented. In the first place the 13 tomographic sections

of the Thetis-2 experiment were analyzed individually. Travel-time observables were modeled using the peak-arrival approach and inverted using the matched-peak inversion approach. An adaptive scheme was used for treating the non-linearity of the model relations, in which the background state (linearization reference) was treated as an unknown of the problem. As an alternative, one could think of using a time-variable background state, set *a priori* from the climatology;¹⁷ this approach would be sufficient for small deviations of the actual state from the climatology. However, for the case of the Thetis-2 experiment the deviations are significant, as shown in Fig. 6, and the use of climatologically constrained background states could bias the inversion results.

By combining slice inversion results from the 13 sections and exploiting the knowledge of the temperature covariance structure for the western Mediterranean basin, estimates for the evolution of the three-dimensional average temperature for the western Mediterranean sub-basin from 1° E to 9° E for the layers 0–2000 m (heat content) and 600–2000 m (deep-water temperature) were obtained. The accuracy of ocean acoustic tomography (Thetis-2 configuration) for temperature measurement was larger for the deep layer (rms error 0.0038 °C) than for the heat content (rms error 0.0081 °C). While the reduced ocean variability at large depths improves the accuracy of temperature measurements, the smaller horizontal scales of the dominating temperature structures plays a deteriorating role as regards the ability to infer horizontal temperature averages from a given tomographic configuration.

A remarkable agreement between tomography heat-content estimates and the ECMWF heat-flux integral was obtained. In this respect, the results presented here are a significant improvement to previous heat-content results, based on simple analyses of a subset of the Thetis-2 data,⁹ in terms of accuracy (~50% error reduction) and also in terms of agreement with the independent heat-flux data. Heat-flux data describe the transfer of heat through the ocean surface, whereas tomographic data can be used to obtain estimates for the total heat content and, in general, horizontal temperature averages over particular depth layers. Surface heat fluxes and heat content are two terms of the heat-budget equation,¹⁵ which also includes advection as a third term. If the advection term can be estimated (as was the case here), then the other two can be compared to verify their accuracy and consistency, on the basis of the heat-budget equation. In open-ocean applications, however, it is never enough to have only one of these, and, in general, heat-flux, heat-content, and advection data are needed to carry out heat-budget analyses.

Ocean acoustic tomography is depth resolving and can be used for the study of temperature evolution of certain depth layers, and hence the transfer of heat between layers (overturning circulation). Of particular interest is the behavior of the western Mediterranean deep water in the light of previous studies reporting the existence of a warming trend in some parts of the basin.²¹ The CTD data and tomography results are consistent with the hypothesis that the warming trend is widespread over the whole basin. Nevertheless, given the size of the tomography error for the 600–2000 m

layer (0.0038 °C), longer term (≥ 2 -year) measurements would be required to draw reliable conclusions. The error of the tomography estimates for the horizontal average deep-water temperature is ~20% of the rms variability of the temperature measurements conducted during the Poseidon and Suroit cruises (0.02 °C). This means that a transmission across the Thetis-2 tomography array offers an accuracy for the deep-water temperature measurement equivalent to that of the average of 25 independent point samples.

The Thetis-2 tomography experiment was conducted as a pilot experiment for long-term monitoring of the western Mediterranean basin with acoustics. For this reason the locations of most of the moorings were selected to make a cable connection of the instruments to shore feasible. The results presented here demonstrate that tomography has the potential to monitor across the extents of the basin with sufficient temporal resolution as well as resolution in depth.

ACKNOWLEDGMENTS

The Thetis-2 project was supported by the EU MAST-2 program (CT91-0006). The authors would like to thank the anonymous reviewers for helpful comments and suggestions.

- ¹ GCOS-82 (WMO/TD No. 1143), The 2nd report on the adequacy of the global observing systems for climate in support of the UNFCCC, April 2003.
- ² N. R. Smith and C. Koblenz, in *The Ocean Observing System for Climate*, Conference Proceedings, St. Raphael, France, 1999.
- ³ W. H. Munk and C. Wunsch, "Ocean acoustic tomography: A scheme for large scale monitoring," *Deep-Sea Res.* **26A**, 123–161 (1979).
- ⁴ W. H. Munk, P. F. Worcester, and C. Wunsch, *Ocean Acoustic Tomography* (Cambridge University Press, New York, 1995).
- ⁵ V. A. Del Grosso, "New equation for the speed of sound in natural waters (with comparisons to other equations)," *J. Acoust. Soc. Am.* **56**, 1084–1091 (1974).
- ⁶ P. F. Worcester, B. D. Cornuelle, M. A. Dzieciuch, W. H. Munk, B. M. Howe, J. A. Mercer, R. C. Spindel, J. A. Colosi, K. Metzger, T. G. Bird-sall, and A. B. Baggeroer, "A test of basin-scale acoustic thermometry using a large-aperture vertical array at 3250-km range in the eastern North Pacific Ocean," *J. Acoust. Soc. Am.* **105**, 3185–3201 (1999).
- ⁷ B. D. Dushaw, "Inversion of multimegahertz-range acoustic data for ocean temperature," *IEEE J. Ocean. Eng.* **24**, 215–223 (1999).
- ⁸ U. Send, in "Thetis-2: A pilot tomography system for monitoring the western Mediterranean basin," Final Report, EU MAST-2 project CT91-0006, March 1996.
- ⁹ U. Send, G. Krahnemann, D. Mauuary, Y. Desaubies, F. Gaillard, T. Terre, J. Papadakis, M. Taroudakis, E. Skarsoulis, and C. Millot, "Acoustic observations of heat content across the Mediterranean sea," *Nature (London)* **385**, 615–617 (1997).
- ¹⁰ E. K. Skarsoulis, "An adaptive scheme for ocean acoustic tomography of large sound-speed variations," *Proceedings of the 3rd European Conference on Underwater Acoustics*, edited by J. S. Papadakis (Crete University, Press, Herakion, 1996), pp. 803–808.
- ¹¹ G. A. Athanassoulis and E. K. Skarsoulis, "Arrival-time perturbations of broadband tomographic signals due to sound-speed disturbances. A wave theoretic approach," *J. Acoust. Soc. Am.* **97**, 3575–3588 (1995).
- ¹² E. K. Skarsoulis, G. A. Athanassoulis, and U. Send, "Ocean acoustic tomography based on peak arrivals," *J. Acoust. Soc. Am.* **100**, 797–813 (1996).
- ¹³ E. K. Skarsoulis, "A matched-peak inversion approach for ocean acoustic travel-time tomography," *J. Acoust. Soc. Am.* **107**, 1324–1332 (2000).
- ¹⁴ E. K. Skarsoulis, "Multi-section matched-peak tomographic inversion with a moving source," *J. Acoust. Soc. Am.* **110**, 786–797 (2001).
- ¹⁵ G. L. Pickard and W. J. Emery, *Descriptive Physical Oceanography*, 5th ed. (Pergamon, Oxford, 1990).
- ¹⁶ H. Lacombe and C. Tchernia, "Caractères hydrologiques et circulation des eaux en Méditerranée," in *The Mediterranean Sea*, edited by D. J. Stanley (Dowden, Hutchinson & Ross, Stroudsburg, 1972), pp. 26–36.

- ¹⁷B. D. Dushaw, P. F. Worcester, B. D. Cornuelle, and B. M. Howe, "Variability of heat content in the central north Pacific in summer 1987 determined from long-range acoustic transmissions," *J. Phys. Oceanogr.* **23**, 2650–2666 (1993).
- ¹⁸E. K. Skarsoulis and U. Send, "One-step analysis of non-linear travel-time data in ocean acoustic tomography," *J. Atmos. Ocean. Technol.* **17**, 240–254 (2000).
- ¹⁹K. D. Leaman and F. Schott, "Hydrographic structure of the convection regime in the Gulf of Lions: Winter 1987," *J. Phys. Oceanogr.* **21**, 573–596 (1991).
- ²⁰G. Madec, M. Crepon, and M. Chartier, "The effect of thermohaline forcing variability on deep water formation in the western Mediterranean Sea: a high-resolution three-dimensional numeric study," *Dyn. Atmos. Oceans* **15**, 301–332 (1991).
- ²¹J. P. Bethoux, B. Gentili, J. Raunet, and D. Tailliez, "Warming trend in the western Mediterranean deep water," *Nature (London)* **347**, 660–662 (1990).